Journal of Biomedical Optics

BiomedicalOptics.SPIEDigitalLibrary.org

Second derivative multispectral algorithm for quantitative assessment of cutaneous tissue oxygenation

Jiwei Huang
Shiwu Zhang
Surya Gnyawali
Chandan K. Sen
Ronald X. Xu

SPIE.

Journal of Biomedical Optics 20(3), 036001 (March 2015)

Second derivative multispectral algorithm for quantitative assessment of cutaneous tissue oxygenation

Jiwei Huang,[a] Shiwu Zhang,[b] Surya Gnyawali,[c] Chandan K. Sen,[c] and Ronald X. Xu[a,b,*]
[a]The Ohio State University, Department of Biomedical Engineering, Columbus, Ohio 43210, United States
[b]University of Science and Technology of China, Department of Precision Machinery and Precision Instrumentation, Hefei, Anhui 230027, China
[c]The Ohio State University, Department of Surgery, Columbus, Ohio 43210, United States

Abstract. We report a second derivative multispectral algorithm for quantitative assessment of cutaneous tissue oxygen saturation (StO_2). The algorithm is based on a forward model of light transport in multilayered skin tissue and an inverse algorithm for StO_2 reconstruction. Based on the forward simulation results, a parameter of a second derivative ratio (SDR) is derived as a function of cutaneous tissue StO_2. The SDR function is optimized at a wavelength set of 544, 552, 568, 576, 592, and 600 nm so that cutaneous tissue StO_2 can be derived with minimal artifacts by blood concentration, tissue scattering, and melanin concentration. The proposed multispectral StO_2 imaging algorithm is verified in both benchtop and *in vivo* experiments. The experimental results show that the proposed multispectral imaging algorithm is able to map cutaneous tissue StO_2 in high temporal resolution with reduced measurement artifacts induced by different skin conditions in comparison with other three commercial tissue oxygen measurement systems. These results indicate that the multispectral StO_2 imaging technique has the potential for noninvasive and quantitative assessment of skin tissue oxygenation with a high temporal resolution. [DOI: 10.1117/1.JBO.20.3.036001]

Keywords: oxygen saturation; multispectral imaging; second derivative spectrum; Monte Carlo; diffuse reflectance.

Paper 140572RR received Sep. 5, 2014; accepted for publication Jan. 20, 2015; published online Mar. 2, 2015.

1 Introduction

Tissue oxygen saturation (StO_2) is a relative measure of the amount of oxygen carried by hemoglobin in biological tissue. Measuring StO_2 will provide important information about tissue viability and help clinicians to make critical decisions in many clinical procedures, such as wound healing management, plastic surgery, and organ transplantation. Various methods, such as blood oxygen level dependent magnetic resonance imaging, pulse oximetry, phosphorescence, electroparamagnetic resonance, and microelectrode, have been used for detecting tissue oxygen content and hemodynamics.[1–3] Among these oximetry techniques, optical oximetry is able to monitor tissue StO_2 continuously and noninvasively by detecting characteristic spectra of oxy-hemoglobin and deoxy-hemoglobin.[4] Commonly used optical oximetry devices are based on contact and single-point measurements of spectral reflectance or transmission in the visible and near-infrared wavelength ranges.[2,5–8] This operation mode may not be suitable for some clinical applications where a sterile environment is required. For example, chronic wound management requires the accurate assessment of wound margin and appropriate detection of tissue viability without contamination to the disease area. Therefore, a noncontact method is preferred for cutaneous tissue StO_2 assessment. In addition, tissue StO_2 assessment in an imaging mode offers several clinical advantages over that of single-point detection. Considering that StO_2 varies spatially in not only suspicious lesions but also healthy tissues,[9–12] imaging tissue StO_2 distribution will help to characterize tissue heterogeneities, identify embedded lesions, and guide therapeutic procedures. Multiple multispectral, hyperspectral, and other advanced imaging techniques have been investigated in recent years for noncontact imaging of skin tissue StO_2.[13–17] These techniques collect skin tissue reflectance at multiple wavelengths, unmix the absorption components of oxy-hemoglobin and deoxy-hemoglobin, and derive the tissue StO_2 map by various reconstruction algorithms.[15,18,19] However, tissue StO_2 maps acquired by various optical oximetry techniques are only relative indicators of tissue metabolism and viability. Accurate interpretation of tissue optical properties into absolute oxygenation levels is challenged by many experimental, physical, and biological limitations.[20–22] In this paper, we define various sources that cause deviations of the measured StO_2 values away from their actual values as artifacts. A variety of artifacts contribute to the lack of accuracy in tissue StO_2 measurements. The static artifacts introduce bias in StO_2 measurements. The dynamic artifacts (including motion artifacts) introduce temporal variations and fluctuations in StO_2 measurements. The static artifacts can be further divided into at least three categories. First, the physical principle limitations for an optical oximetry technique, such as the scattering of light in biologic tissue and the wavelength-dependent depth of light penetration in tissue, hinder the accurate interpretation of physiologic parameters from optical measurements. Second, variations in imaging hardware and test conditions, such as nonuniform illumination and specular reflectance conditions, introduce further artifacts in StO_2 measurement. Finally, intrapatient and interpatient variations in tissue physiologic conditions and chromophore concentrations also significantly affect the accuracy of StO_2 imaging. For example, skin pigments and chromophores other than oxy-hemoglobin and deoxy-hemoglobin contribute to heterogeneous background absorption at different

---

*Address all correspondence to: Ronald X. Xu, E-mail: xu.ronald@hotmail.com

1083-3668/2015/$25.00

skin sites and interpatient variation in skin color.[21] Previous studies also show that oxy-hemoglobin, deoxy-hemoglobin, and scattering vary significantly for patients in different ethnic groups or for the same patient at different skin sites.[23,24] In this paper, we focus on a multispectral imaging algorithm that may effectively reduce the StO_2 mapping artifacts introduced by other skin chromophores. At the current status of research, we have not studied the systemic methods for effective elimination of motion artifacts and other types of artifacts yet.

In an effort to minimize the artifacts for cutaneous tissue StO_2 measurement, various algorithms have been explored. Seo et al. used a linear model of oxy-hemoglobin and deoxy-hemoglobin with a modulation of scattering and melanin to approximate the absorption spectrum of skin tissue in the wavelength range from 520 to 585 nm.[25] Stamatas et al. calculated the melanin concentration, corrected the absorption spectrum, and then it fitted into the absorption spectra of oxy-hemoglobin and deoxy-hemoglobin.[26,27] Mansfield et al. analyzed the skin reflectance spectrum by fuzzy C-means clustering and then applied a four-term linear regression fitting with oxy-hemoglobin, deoxy-hemoglobin, offset, and slope terms.[28–30] Sowa et al. reduced the bias from melanin by applying an orthogonal subspace projection method for hyperspectral image classification.[31,32] Nishidate et al. determined the optical path lengths of different absorbers by inverse Monte Carlo simulation and applied the results to a multiple regression algorithm to find the fitting coefficients for oxy-hemoglobin, deoxy-hemoglobin, and melanin.[33] Jakovels and Spigulis used multiple Gaussian and exponential functions to fit the absorption spectra for oxy-hemoglobin, deoxy-hemoglobin, and melanin, and then approximated the skin tissue optical density spectrum from 500 to 700 nm by nonlinear least square approximation.[15] Despite these advances, no systemic study has been carried out for quantitative study and evaluation of reliable algorithms for cutaneous tissue StO_2 measurement at different skin conditions. Consequently, many existing hyperspectral and multispectral imaging devices can only provide relative information about tissue StO_2 vulnerable to skin conditions.

This paper reports a multispectral algorithm for noncontact, quantitative and high temporal resolution imaging of cutaneous tissue StO_2 with reduced measurement artifacts in comparison with conventional imaging methods. The multispectral algorithm is studied numerically in a simplified skin tissue model that only considers lipid and primary chromophores, such as oxy-hemoglobin, deoxy-hemoglobin, and melanin. Other chromophores, such as glucose, keratin, and bilirubin, are neglected at the current stage of research. The algorithm is also validated experimentally in a phantom system that consists of whole blood, lipid, and India ink. India ink is used to simulate different skin types since it has been adopted by many researchers to mimic the absorption properties of melanin.[34,35] In Sec. 2.1, reflectance spectra of skin tissue at different StO_2, scattering, blood, and melanin conditions are simulated by an empirical light transport model with a semi-infinite boundary condition. A parameter of the second derivative ratio (SDR) is derived as the function of tissue StO_2 based on the simulated reflectance spectra and the method of wide-gap second derivative spectroscopy. An optimal set of wavelengths is defined so that the SDR value is monotonically determined by skin tissue StO_2 regardless of the tissue condition variations. In Sec. 2.2, the proposed multispectral imaging method is verified in tissue-simulating phantoms, where bovine blood, intralipid, and ink are mixed at different concentrations. Clinical feasibility of imaging skin tissue StO_2 is demonstrated on a healthy human subject following a postocclusive reactive hyperemia (PORH) protocol. During the PORH procedure, multispectral images are acquired at the specific set of wavelengths and the tissue SDRs are derived at each pixel for continuous mapping of tissue StO_2. To demonstrate that our StO_2 algorithm is less vulnerable to skin condition variations, 10 human subjects with different skin types were recruited and their skin StO_2 was measured by our multispectral imaging system. Statistical analysis shows that skin type does not significantly affect the StO_2 measurement by our system. To test the effect of additional background absorption on cutaneous StO_2 measurement, a portion of a human subject's forearm is painted with India ink and multispectral images are acquired within and outside the painted skin area at six designated wavelengths. The reconstructed StO_2 map is compared with that of a commercial OxyVu hyperspectral imaging system (HyperMed Imaging, Inc.).[30] Reconstructed StO_2 values within and outside the painted area are compared with those by the OxyVu system. The experimental results are discussed in Sec. 3, followed by conclusions drawn from these results.

2 Materials and Methods

2.1 *Imaging Algorithms*

Multispectral imaging of skin tissue StO_2 is achieved by successive algorithms of forward simulation and inverse reconstruction. The forward model simulates light transport in semi-infinite biologic tissue at different blood, scattering, melanin, and StO_2 conditions, with tissue parameters calibrated by Monte Carlo simulation. The inverse model reconstructs tissue parameters based on the analytical expression of SDRs at the designated wavelengths.

2.1.1 *Forward simulation*

Skin has a physiologic structure that can be divided into seven layers. Table 1 lists major tissue parameters of each skin layer, including thickness (d), volume fraction of hemoglobin in blood (r), and concentrations of blood (C_{blood}), water (C_{water}), fat (C_{fat}), and melanin (C_{melanin}).[36–38] Traditionally, Monte Carlo modeling is used to simulate light transport in multilayered biologic tissue.[39] However, this method is time-consuming and is not appropriate for inverse reconstruction. Therefore, a simplified diffuse reflectance model with a semi-infinite boundary condition is introduced.[40] The absorption and scattering properties in this simplified model are averaged across different skin layers in order to fit in the semi-infinite boundary condition, while the multilayer tissue condition was used in Monte Carlo modeling. First of all, the absorption of any skin layer, μ_{ai} ($i = 1$ to 7), is denoted as the sum of absorptions from different absorbers, including oxygenated-hemoglobin (μ_a^{HbO}), deoxygenated-hemoglobin (μ_a^{Hb}), melanin (μ_a^{mel}), water (μ_a^{water}), fat (μ_a^{fat}), and a baseline without any absorbers (μ_a^{base}):

$$\mu_{ai} = \mu_{ai}^{\mathrm{HbO}} + \mu_{ai}^{\mathrm{Hb}} + \mu_{ai}^{\mathrm{mel}} + \mu_{ai}^{\mathrm{water}} + \mu_{ai}^{\mathrm{fat}} + \mu_{ai}^{\mathrm{base}}, \tag{1}$$

where

$$\mu_{ai}^{\mathrm{HbO}} = 2.303\varepsilon^{\mathrm{HbO}} \cdot \mathrm{StO}_2 \left(\frac{C_{\mathrm{Hb}}}{\mathrm{M.W.}_{\mathrm{Hb}}} C_i^{\mathrm{blood}} \right), \tag{2}$$

Table 1 Properties of seven skin layers obtained and calculated from previous publications.[36–38] d is the thickness of the layer; r is the volume fraction of hemoglobin in blood; C_{blood}, C_{water}, C_{fat}, and C_{melanin} are the volume fractions of blood, water, fat, and melanin in each layer; g, n, and μ_s are anisotropy factor, refractive index, and scattering coefficient of each layer measured at 633 nm.

Skin layers	d(μm)	C_{blood}	r	C_{water}	C_{fat}	C_{melanin}	g	n	μ_s (mm^{-1})
Stratum corneum	20	0	0	0.05	0	0	0.86	1.5	100
Living epidermis	80	0	0	0.2	0	0.02 (Caucasians); 0.13 (Asians); 0.3 (Africans)	0.8	1.34	45
Papillary dermis	160	0.04	0.1114	0.5	0	0	0.9	1.4	30
Upper blood net dermis	100	0.3	0.1114	0.6	0	0	0.95	1.34	35
Reticular dermis	1400	0.04	0.1114	0.7	0	0	0.8	1.4	25
Deep blood net dermis	100	0.1	0.1114	0.7	0	0	0.95	1.38	30
Hypodermis	28,140	0.05	0.1114	0.7	0.6	0	0.75	1.44	

$$\mu_{ai}^{\text{Hb}} = 2.303\varepsilon^{\text{Hb}} \cdot (1-\text{StO}_2)\left(\frac{C_{\text{Hb}}}{\text{M.W.}_{\cdot\text{Hb}}} C_i^{\text{blood}}\right), \tag{3}$$

$$\mu_{ai}^{\text{mel}} = \varepsilon^{\text{mel}} \cdot C_i^{\text{mel}}, \tag{4}$$

$$\mu_{ai}^{\text{water}} = \varepsilon^{\text{water}} \cdot C_i^{\text{water}} \cdot (1 - r_i C_i^{\text{blood}}), \tag{5}$$

$$\mu_{ai}^{\text{fat}} = \varepsilon^{\text{fat}} \cdot C_i^{\text{fat}} \cdot (1 - r_i C_i^{\text{blood}}), \tag{6}$$

$$\mu_{ai}^{\text{base}} = \varepsilon^{\text{base}}(1 - C_i^{\text{blood}} - C_i^{\text{mel}} - C_i^{\text{fat}})(1 - r_i C_i^{\text{blood}}). \tag{7}$$

In the above equations, $\text{M.W.}_{\cdot\text{Hb}}$ and C_{Hb} are the molecular weight and total concentration of hemoglobin, respectively. ε^{HbO}, ε^{Hb}, $\varepsilon^{\text{water}}$, and ε^{fat} are the extinction coefficients of the corresponding absorbers obtained from previous studies.[41,42] ε^{mel} is the absorption coefficient of melanin:[38] $\varepsilon^{\text{mel}} = 1.7 \times 10^{12}\lambda^{-3.48}\ (\text{cm}^{-1})$. $\varepsilon^{\text{base}}$ is the absorption coefficient of skin free of any absorbers:[43] $\varepsilon^{\text{base}} = 7.84 \times 10^{8}\lambda^{-3.255}\ (\text{cm}^{-1})$.

The absorption of the first layer stratum corneum is different from the other layers:[36,37]

$$\mu_a^{\text{stratum}} = (1\text{-}3 \times 10^{-4}\lambda + 0.125\varepsilon^{\text{base}}) \times 0.95 + \varepsilon^{\text{water}} \times 0.05\ (\text{cm}^{-1}). \tag{8}$$

The overall absorption of the whole skin is calculated by taking the weighted average of the absorption of all layers.

$$\mu_a = \sum_{i=1}^{7} \mu_{ai} \cdot f_i, \tag{9}$$

where f_i is defined as the weight factor for the absorption of a specific layer contributing to the overall absorption ($\sum_{i=1}^{7} f_i = 1$). In general, the weight factor of the top layer is greater than that of the bottom layer because light attenuates exponentially with the tissue depth. These weight factors are determined by matching the simulated skin reflectance by the diffuse transport model with that by Monte Carlo modeling, as described in Appendix A. Different weight factors are derived for different skin conditions.

The reduced scattering coefficient of the whole skin μ_s' is approximated by the following equation based on *in vivo* measurements:[23,44]

$$\mu_s' = 1.1 \times 10^{12}\lambda^{-4} + 73.7\lambda^{-0.22}\ (\text{cm}^{-1}). \tag{10}$$

The diffuse reflectance R is calculated by the following approximation algorithm:[40]

$$R = R_s + \frac{(1-R_s)(1\text{-}s)(1-b_1 s)}{1+b_2 s}, \quad \text{in which } s = \sqrt{\frac{\mu_a}{\mu_a + \mu_s'}}. \tag{11}$$

In the above equations, $R_s = (n-1)^2/(n+1)^2$ is the specular reflectance; n is refractive index ($n = 1.4$ for typical biologic tissue); $b_1 = -0.34\text{–}1.1g + 0.68g^2$ and $b_2 = 4.11\text{–}2.77g + 2.27g^2$ are two constants; g is an anisotropy factor.

Finally, since our experiment used an optical filter with a bandwidth of 7 nm (Sec. 2.2.1), the resultant reflectance spectrum was corrected accordingly. The transmission of the filter with a bandwidth FWHM is assumed to be a Gaussian shape:

$$G(\lambda_0 - \lambda) = \frac{2\sqrt{\ln 2/\pi}}{\text{FWHM}} \cdot e^{-4\ \ln\ 2 \cdot \left(\frac{\lambda-\lambda_0}{\text{FWHM}}\right)^2}. \tag{12}$$

The reflectance spectrum $R(\lambda_0)$ measured using this filter was calculated as the convolution of $G(\lambda_0 - \lambda)$ and the original reflectance spectrum $R(\lambda)$.

$$R(\lambda_0) = R(\lambda) \otimes G(\lambda_0 - \lambda) = \int_{\lambda_0-3\sigma}^{\lambda_0+3\sigma} R(\lambda) \cdot G(\lambda_0 - \lambda)\text{d}\lambda. \tag{13}$$

The above forward algorithm is used to simulate diffuse reflectance measurements at 450 skin conditions, including the combinations of five blood concentration levels ($C_{\text{blood}} = 0.8$, 0.9, 1, 1.1, 1.2 of normal C_{blood}), three melanin concentrations ($C_{\text{melanin}} = 0.02$, 0.13, and 0.3 in living epidermis, corresponding to Caucasians, Asians, and Africans), five scattering levels ($\mu_s' = 0.8$, 0.9, 1, 1.1, 1.2 of typical μ_s'), and six oxygen saturation levels ($StO_2 = 0$, 20%, 40%, 60%, 80%, 100%). The diffuse reflectance R as a function of λ, C_{blood}, C_{melanin}, μ_s', and StO_2 is simulated in the wavelength range from 500 to 650 nm. Figures 1(a), 1(b), and 1(c) show the skin reflectance spectra at three melanin concentrations and different levels of StO_2, scattering, and blood concentration, respectively. According to Fig. 1, the dc offset of the skin reflectance of all wavelengths is affected by melanin concentration, scattering, and blood concentration. Among these three factors, the effect of melanin is over 10 times more significant than those of the other two factors. On the other hand, the shape of the spectrum is mainly determined by StO_2, regardless of variations in scattering, blood concentration, and melanin concentration. This observation indicates the possibility of using multispectral imaging to analyze the shape of reflectance spectra and mapping tissue StO_2 with a minimal measurement bias from other tissue components.

2.1.2 *Reconstruction of tissue StO_2*

A multispectral second derivative algorithm is developed to reconstruct skin tissue StO_2 based on the reflectance measurements at six designated wavelengths. The algorithm follows consecutive steps of calculating the absorption-scattering ratio, deriving wide-gap second derivative, obtaining an analytical expression of SDR, and curve fitting for StO_2 calculation. First, the ratio between absorption and reduced scattering coefficients ($r = \mu_a/\mu_s'$) is calculated by transforming Eq. (11):

$$r = \frac{\mu_a}{\mu_s'} = \frac{s^2}{1 - s^2}, \tag{14}$$

where $b_1 \cdot s^2 - (b_1 + R_1 \cdot b_2 + 1) \cdot s + (1 - R_1) = 0$ and $R_1 = (R - R_s)/(1 - R_s)$.

After that, a wide-gap second derivative spectroscopic method is used to derive the second derivative of absorption-scattering ratio $rr(\lambda)''$ as a function of the wavelength λ and the wavelength gap $\delta\lambda$:[45]

$$rr(\lambda)'' = [r(\lambda + \delta\lambda) + r(\lambda - \delta\lambda) - 2r(\lambda)]/(2\delta\lambda). \tag{15}$$

The SDR is then expressed as the ratio between $rr(\lambda_1)''$ and $rr(\lambda_2)''$:

$$\begin{aligned}\text{SDR}(\lambda_1, \lambda_2) &= \frac{rr(\lambda_1)''}{rr(\lambda_2)''} \\ &= \frac{r(\lambda_1 + \delta\lambda) + r(\lambda_1 - \delta\lambda) - 2r(\lambda_1)}{r(\lambda_2 + \delta\lambda) + r(\lambda_2 - \delta\lambda) - 2r(\lambda_2)}.\end{aligned} \tag{16}$$

After substituting the absorption-scattering ratio r with μ_a/μ_s' and neglecting higher-order terms as described in Appendix B, one can derive the approximated analytical expression of $\text{SDR}(\lambda_1, \lambda_2)$:

$$\text{SDR}(\lambda_1, \lambda_2) = \frac{\mu_s'(\lambda_2)}{\mu_s'(\lambda_1)} \cdot \frac{[(\varepsilon^{\text{HbO}})''_{\lambda_1} - (\varepsilon^{\text{Hb}})''_{\lambda_1}]StO_2 + (\varepsilon^{\text{Hb}})''_{\lambda_1}}{[(\varepsilon^{\text{HbO}})''_{\lambda_2} - (\varepsilon^{\text{Hb}})''_{\lambda_2}]StO_2 + (\varepsilon^{\text{Hb}})''_{\lambda_2}}. \tag{17}$$

According to Eq. (17), $\text{SDR}(\lambda_1, \lambda_2)$ varies with skin tissue StO_2 and the scattering coefficients at wavelengths λ_1 and λ_2. In the case when these two wavelengths differ from each other by <10 nm, $\mu_s'(\lambda_1) \approx \mu_s'(\lambda_2)$ and $\text{SDR}(\lambda_1, \lambda_2)$ is primarily determined by tissue StO_2. The wavelength pair of (λ_1, λ_2) can be optimized for one-to-one mapping between SDR and StO_2 with a minimal bias induced by different skin conditions. To identify the optimal wavelength pair, all the possible SDRs are calculated at different skin conditions for the wavelength pairs ranging from 500 to 650 nm and with the wavelength difference of 8 and 10 nm, respectively. The calculated SDRs are screened and the optimal wavelength set is found to be $\lambda_1 = 568$ nm, $\lambda_2 = 576$ nm, and $\delta\lambda = 24$ nm. According to Eq. (16), in total, six wavelengths are involved in the calculation of $\text{SDR}(568,576)_{(\delta\lambda=24)}$: 544, 552, 568, 576, 592, and 600 nm. Table 2 lists the SDR(568, 576) values at 12 representative skin tissue conditions selected from all the 450 conditions as described at the end of Sec. 2.1.1. The SDR level at 20% StO_2 is 0.872(±0.004) averaged from 450 tissue conditions of different levels of blood concentration, melanin concentration, and scattering. Similarly, the SDR level at 80% StO_2 is 0.396(±0.003). The overall relationship between SDR and StO_2 can be approximated by the following monotonic function:

$$StO_2 = 100(-1.4\text{SDR}^3 + 4.82\text{SDR}^2 - 5.66\text{SDR} + 2.38). \tag{18}$$

Figure 2 plots the above monotonic function where skin tissue StO_2 can be derived by taking the reflectance measurements

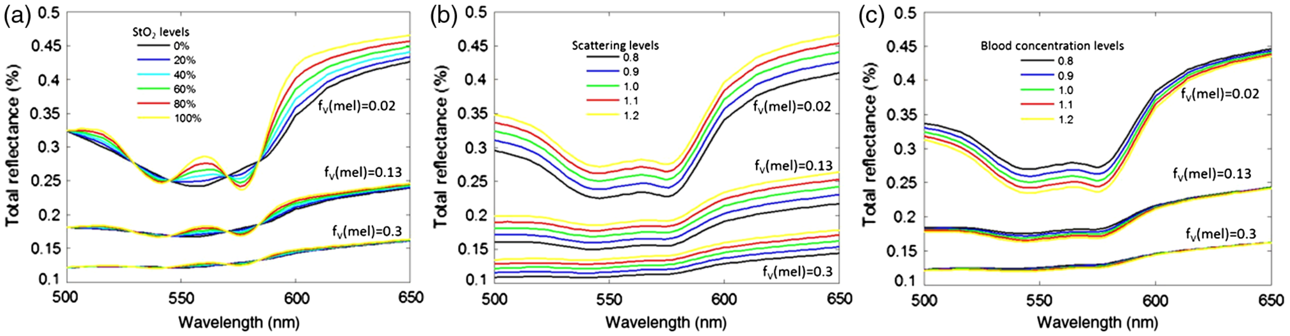

Fig. 1 Spectral reflectance of skin tissue at different conditions simulated by a forward algorithm. (a) Reflectance spectra at six StO_2 levels, three melanin concentrations, and fixed blood and scattering conditions. (b) Reflectance spectra at five scattering levels, three melanin concentrations, and fixed StO_2 and blood concentration conditions. (c) Reflectance spectra at five blood concentration levels, three melanin concentrations, and fixed StO_2 and scattering conditions.

Table 2 Second derivative ratio [SDR(568,576)$_{(\delta\lambda=24)}$] of 12 skin tissue conditions. The definitions of skin conditions were described in Sec. 2.1.1.

Different skin tissue conditions				
Blood level	Melanin level	Scattering level	StO_2 (%)	SDR
0.8	0.13	1	20	0.870
1.2	0.13	1	20	0.872
1	**0.02**	1	20	0.877
1	**0.3**	1	20	0.868
1	0.13	**0.8**	20	0.872
1	0.13	**1.2**	20	0.871
0.8	0.13	1	80	0.395
1.2	0.13	1	80	0.397
1	**0.02**	1	80	0.400
1	**0.3**	1	80	0.392
1	0.13	**0.8**	80	0.396
1	0.13	**1.2**	80	0.396

at the designated wavelengths (i.e., 544, 552, 568, 576, 592, and 600 nm) and calculating the SDR (568, 576) using Eqs. (15) and (16).

2.2 *Experiments*

2.2.1 *Multispectral imaging system*

A multispectral imaging system with a hyperspectral imaging capability is constructed for quantitative imaging of skin tissue StO_2. A Hamamatsu ORCA ER deep cooling CCD camera (Hamamatsu, Bridgewater, New Jersey) with a camera lens (Edmund optics, Barrington, New Jersey) is used for image acquisition. A Varispec liquid crystal tunable filter (Cambridge Research Inc., Cambridge, Massachusetts) with a working wavelength range of 400 to 720 nm and a bandwidth of 7 nm is mounted in front of the camera for multispectral imaging. An OSL1 fiber light source (Thorlabs, Newton, New Jersey) provides broadband optical illumination to the test object. A user interface is programmed by Labview Professional Development System (National Instruments, Austin, Texas) for equipment control, synchronization, and image acquisition tasks.

For quantitative assessment of skin tissue StO_2, multispectral images are acquired at 544, 552, 568, 576, 592, and 600 nm on skin tissue and on a National Institute of Standards and Technology traceable white diffuser. The reflectance map at each wavelength $R(\lambda)$ is calculated by taking the ratio of the skin and the diffuser measurements pixel by pixel. After that, the SDR value is calculated using Eqs. (15) and (16). Finally, the StO_2 map of skin tissue is obtained by Eq. (18).

Since the measurement of reflectance $R(\lambda)$ required multispectral images of both skin and the white diffuser, the intensity of the light source has to be stable during the acquisition of these two groups of images. Thus, the light source was turned on for 10 min before any measurement was taken. An "auto exposure" function was developed in the Labview user interface and the camera exposure time was calibrated on the white diffuser to ensure that the gray level of the 8-bit image was always 235 at each wavelength.

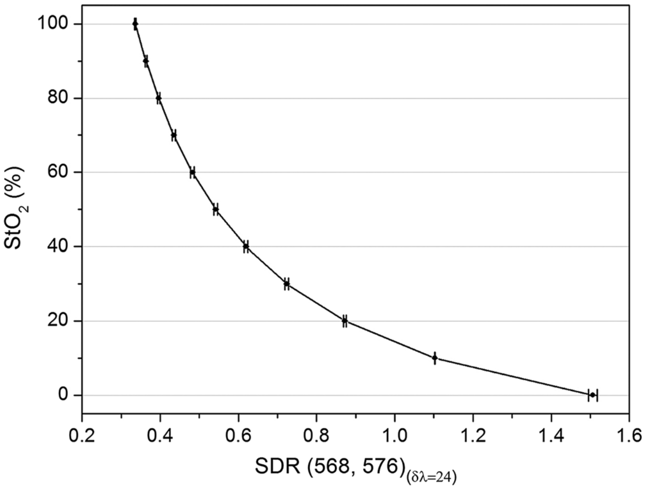

Fig. 2 Oxygen saturation of skin StO_2 versus SDR(568,576)$_{(\delta\lambda=24)}$. The error bar in the plot indicates the variation due to different blood concentration, melanin concentration, and scattering of skin.

2.2.2 *Algorithm verification on tissue-simulating phantoms*

The StO_2 algorithm is verified using a liquid blood phantom. The phantom is prepared by mixing fresh bovine blood, India ink (Sanford, Bellwood, Illinois), and 10% Intralipid (Henry Schein Inc., Melville, New York) in phosphate buffered saline (PBS, Fisher Scientific, Newton, New Jersey). First, a base phantom is prepared by mixing 2.5 mL of blood, 4 mL of Intralipid, and 30 μL of India ink in PBS solution to a total volume of 200 mL. Different skin tissue conditions are simulated by adding additional recipe components to the base phantom. For example, different levels of blood concentration, scattering, and skin darkness are simulated by adding 20% more blood, 20% more Intralipid, and 100% more India ink to the base phantom, respectively. The pH level of the phantom is adjusted to 7.4 by adding NaOH and HCl. The oxygenation level of the phantom is adjusted by the dropwise addition of sodium hydrosulfite at a concentration of 0.1 g/mL.

The phantom StO_2 is measured by the multispectral imaging method as described in the previous section and compared with a hyperspectral imaging method as described in Ref. 25. To eliminate the measurement artifact induced by ambient oxygen, the blood phantom is placed in a cardboard container and ventilated with argon gas. During the test, eight oxygenation plateaus ranging from ~100% to ~0% are achieved by the dropwise addition of sodium hydrosulfite. At each oxygenation plateau, the blood phantom is mixed to homogeneity by a stir bar. Hyperspectral images are acquired from 500 to 600 nm at a spectral resolution of 2 nm. Among them, images at 544, 552, 568, 576, 592, and 600 nm are used to reconstruct the StO_2 map following our multispectral imaging algorithm. In comparison, a hyperspectral imaging algorithm uses the whole reflectance spectra to reconstruct tissue StO_2.

2.2.3 *Algorithm verification on a human subject*

The multispectral imaging algorithm is verified by human subject testing following a clinical protocol approved by the Ohio State University IRB (Protocol No: 2010H0017). The test measures the forearm tissue StO_2 of a healthy male volunteer in response to a postocclusive reactive hyperemia (PORH) procedure.[46] The PORH protocol consists of a preocclusive baseline period of 2 min without compression, a supersystolic occlusion period of 2 min with a compression load of 50 mmHg above the systolic pressure applied to the arm by a pressure cuff, and a reactive hyperemia period of 2 min without compression. During the PORH test, multispectral images are acquired continuously. In the meantime, deep tissue oxygen saturation and skin oxygen tension on the same arm are measured by an OxiplexTS tissue spectrophotometer (ISS Inc., Urbana Champaign, Illinois) and a TCM transcutaneous oxygen monitor (Radiometer, Denmark), respectively. The skin tissue StO_2 levels obtained by multispectral imaging are compared with the OxiplexTS and the TCM measurements.

2.2.4 *Measuring StO_2 of in vivo skin of different skin types*

In order to evaluate the effect of skin type on oxygenation measurement, a total of 10 subjects with different skin types were recruited for continuous imaging of skin StO_2 following the PORH protocol. Among these 10 subjects, five are Caucasians and light tanned Hispanos, who have the lowest melanin levels; three are Asians with medium melanin levels; and two are darkly pigmented Asians with the highest melanin levels. The test procedure of each subject was the same as that described in Sec. 2.2.3. The influence of skin types on multispectral imaging of skin oxygenation was evaluated statistically and compared with the OxiplexTS tissue spectrophotometer and the TCM transcutaneous oxygen monitor measurements.

2.2.5 *Measuring StO_2 of in vivo skin with additional background absorption*

We have also tested *in vivo* whether the proposed multispectral imaging algorithm is able to reduce the StO_2 measurement bias owing to background absorption variations. A portion of the subject's forearm within the field of view is painted with 1% India ink dissolved in ethanol to simulate the darker skin color. Multispectral images are acquired with the field of view covering both the ink-painted area and the surrounding normal tissue. In comparison, the same experiment is repeated at the same skin location on the same subject using an OxyVu hyperspectral imaging system. The reconstructed StO_2 maps by these two imaging systems are compared side by side.

3 Results and Discussion

The multispectral imaging algorithm is verified by benchtop testing on a tissue-simulating phantom with different oxygenation levels. At each oxygenation level, multispectral images are acquired at the wavelengths of 544, 552, 568, 576, 592, and 600 nm. The diffuse reflectance measurements are averaged within three regions of interest (ROIs) for multispectral reconstruction of StO_2. Figure 3 plots the reconstructed StO_2 values versus those derived from the previously reported hyperspectral method.[25] According to the figure, our multispectral algorithm yields the StO_2 values linearly correlated with the hyperspectral algorithm. Moreover, StO_2 measurements at four simulated skin conditions (i.e., standard recipe, +20% lipid, +20% blood, and +100% ink) fall into a diagonal line, indicating that our StO_2 reconstruction algorithm is not vulnerable to variations in skin tissue parameters, such as blood concentration, scattering, and background absorption.

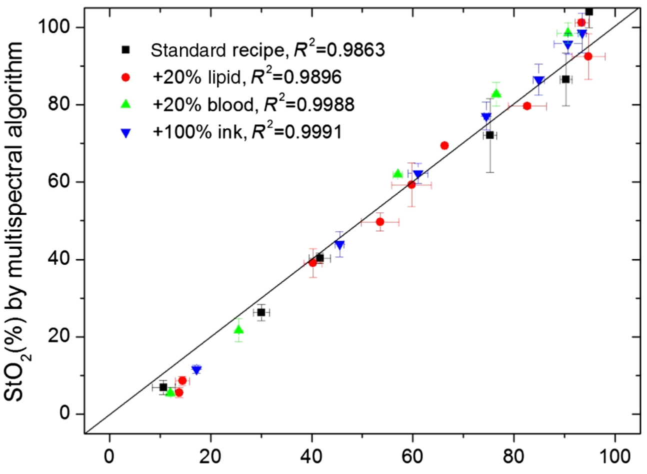

Fig. 3 Oxygen saturation of blood phantom measured by multispectral algorithm proposed in this paper versus that measured by hyperspectral imaging method of Ref. 25.

The multispectral imaging algorithm is also verified by human subject testing. Figure 4 shows the gray-scale image of the tested arm and the reconstructed StO_2 maps during the PORH procedure. According to the figure, the skin StO_2 level is in the range of 40 to 50% at the baseline condition before vascular occlusion [Fig. 4(b)], which is coincident with the previous study.[47] As the blood vessel is occluded, the skin StO_2 level drops to <10% [Fig. 4(c)]. After the occlusion is released, the skin StO_2 level increases to >60% due to hyperemia [Fig. 4(d)]. At the end of the test, the StO_2 level resumes its baseline value [Fig. 4(e)]. The StO_2 dynamics detected during a PORH procedure is consistent with the previous report.[17]

The StO_2 dynamics of cutaneous tissue during a PORH procedure is compared with simultaneous measurements of deep tissue oxygenation and transcutaneous tissue oxygen tension. Figure 5(a) illustrates the test protocol where a baseline period of 2 min is followed by a suprasystolic occlusion period of 2 min, and then a reactive hyperemia period of 2 min. Figure 5(b) plots the corresponding dynamic changes of skin tissue StO_2 calculated by averaging 10 selected ROIs in the StO_2 oxygenation map as shown in Fig. 4. Figures 5(c) and 5(d) are simultaneous measurements of deep tissue oxygenation and transcutaneous tissue oxygen tension. According to Fig. 5, the dynamic changes of cutaneous tissue StO_2 coincide well with those of deep tissue oxygenation and transcutaneous oxygen tension.

Skin tissue StO_2 images were acquired on 10 human subjects with different skin types to evaluate the robustness of our multispectral imaging technique at different skin conditions. The tests followed the same PORH protocol as described before. Figure 6 shows the averaged skin StO_2 levels for 10 subjects measured by our multispectral imaging system under the normal condition without vascular occlusion pressure. For each human subject, 10 measurements were carried out to

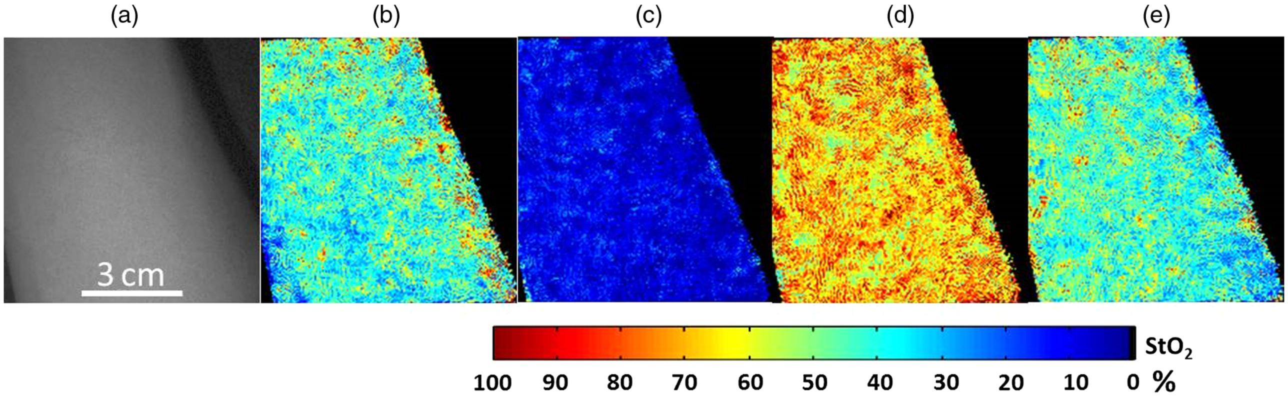

Fig. 4 Picture of the arm (a). Skin oxygenation map before (b), during (c), after vascular occlusion (d), and at the end of the test (e).

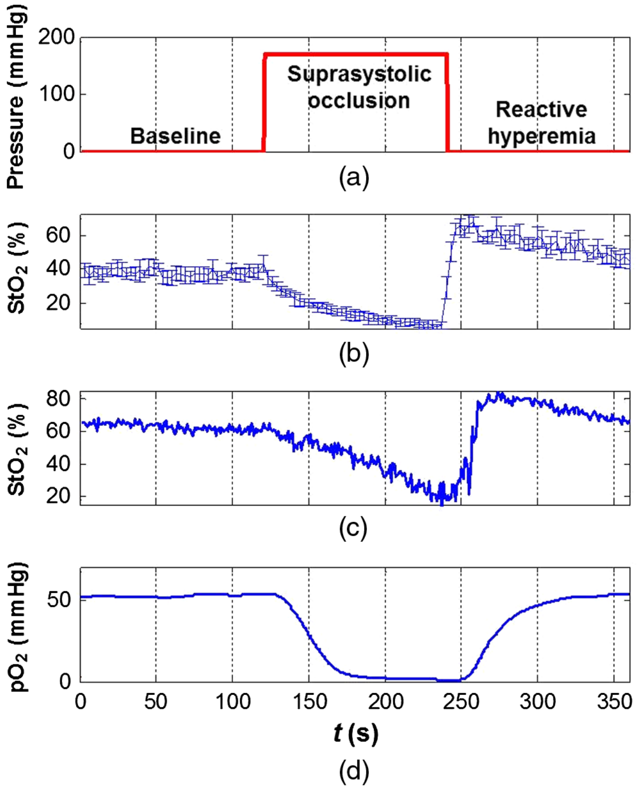

Fig. 5 Postocclusive reactive hyperemia (PORH) test protocol (a), and the history of cutaneous tissue oxygenation (b), deep tissue oxygenation (c), and transcutaneous tissue oxygen tension (d) measured by multispectral imaging, tissue oximeter, and TCM device, respectively.

generate 10 oxygen saturation maps. In each oxygen saturation map (500 × 500 pixels), 10 ROIs of 25 × 25 pixels were randomly drawn in the skin area without hair. In order to avoid measurement artifacts due to arm curvature, these ROIs were all selected away from the edge of the arm. Then the StO$_2$ for a subject was calculated by averaging StO$_2$ values from a total of $10 \times 10 = 100$ ROIs. In order to statistically evaluate the influence of skin darkness on StO$_2$ measurement, an analysis of variance (ANOVA) test was performed. The resultant p value is 0.29, indicating that skin type does not significantly affect the StO$_2$ measurement for our multispectral imaging system.

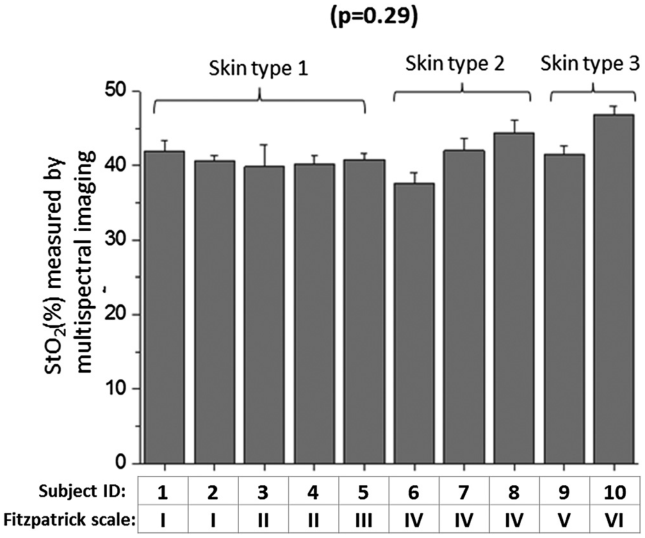

Fig. 6 Averaged skin StO$_2$ of 10 subjects under normal conditions measured by multispectral imaging with our algorithm. The subjects were arranged in the order of skin melanin levels with 1 being the lowest to 10 being the highest. Fitzpatrick scale of each subject is also listed.

Figure 7 shows the averaged skin tissue StO$_2$ (%) acquired by our multispectral imaging system, the deep tissue StO$_2$ (%) acquired by the Oxiplex tissue oximeter, and the transcutaneous oxygen tension pO$_2$ (mmHg) acquired by the TCM device during the PORH procedure on 10 subjects. The error bars indicate the variations among different subjects. During the baseline period (first 2 min), the skin StO$_2$ (%) measured by multispectral imaging system is 42.5($\pm$6.49%); the deep tissue StO$_2$ (%) measured by the tissue oximeter is 55.0($\pm$13.6%); and the transcutaneous oxygen tension pO$_2$ (mmHg) measured by the TCM oxygen monitor is 62.0($\pm$19.7%). These data show that the % standard deviation of StO$_2$ (%) measured by our system is much less than that of the other two measurements. Furthermore, the same ANOVA test was performed on the other two measurements to statistically evaluate the influence of skin type. The p values are both <0.01 for deep tissue StO$_2$ (%) measured by the tissue oximeter and transcutaneous oxygen tension pO$_2$ (mmHg) measured by the TCM oxygen monitor. The above result shows that the measurement by our multispectral imaging system is less biased by skin type than those of the other two oximetry devices.

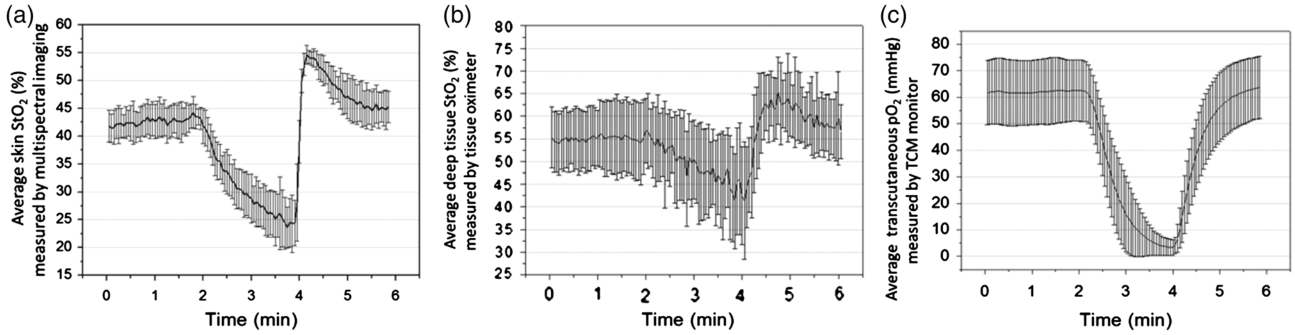

Fig. 7 Measurements of 10 subjects of different skin types during PORH: (a) average skin StO$_2$ (%) measured by our system, (b) deep tissue StO$_2$ (%) measured by Oxiplex tissue oximeter, and (c) transcutaneous oxygen tension pO$_2$ (mmHg) measured by TCM oxygen monitor.

The effect of additional background absorption on cutaneous StO$_2$ measurement is also tested on a human subject. A portion of the subject's forearm is painted with ink to simulate a darker skin. Cutaneous StO$_2$ maps are acquired by both our multispectral imaging system and an OxyVu hyperspectal imaging system. Figures 8(a) and 8(b) show the photographic image of the forearm tissue with the central area painted with ink and the corresponding StO$_2$ map reconstructed by our multispectral algorithm. Two square-shaped ROIs are selected within and outside the ink-painted area, with the cutaneous StO$_2$ levels averaged as 41.6 and 38.1%, respectively, resulting in a measurement difference of 3.5%. In comparison, the same test performed by an OxyVu system on the same arm [Figs. 8(c) and 8(d)] shows an averaged cutaneous StO$_2$ level of 62.7% within the ink-painted skin area and 43.0% outside the area, resulting in a measurement difference of 19.7%. This result presumably indicates that the proposed multispectral algorithm effectively reduces the artifact of additional background absorption on cutaneous StO$_2$ measurement.

The multispectral imaging technique reported in this paper was developed primarily for the noncontact measurement of cutaneous tissue StO$_2$ since the proposed wide-gap second derivative spectral imaging algorithm is sensitive to tissue oxygenation changes. Considering that tissue oxygenation is

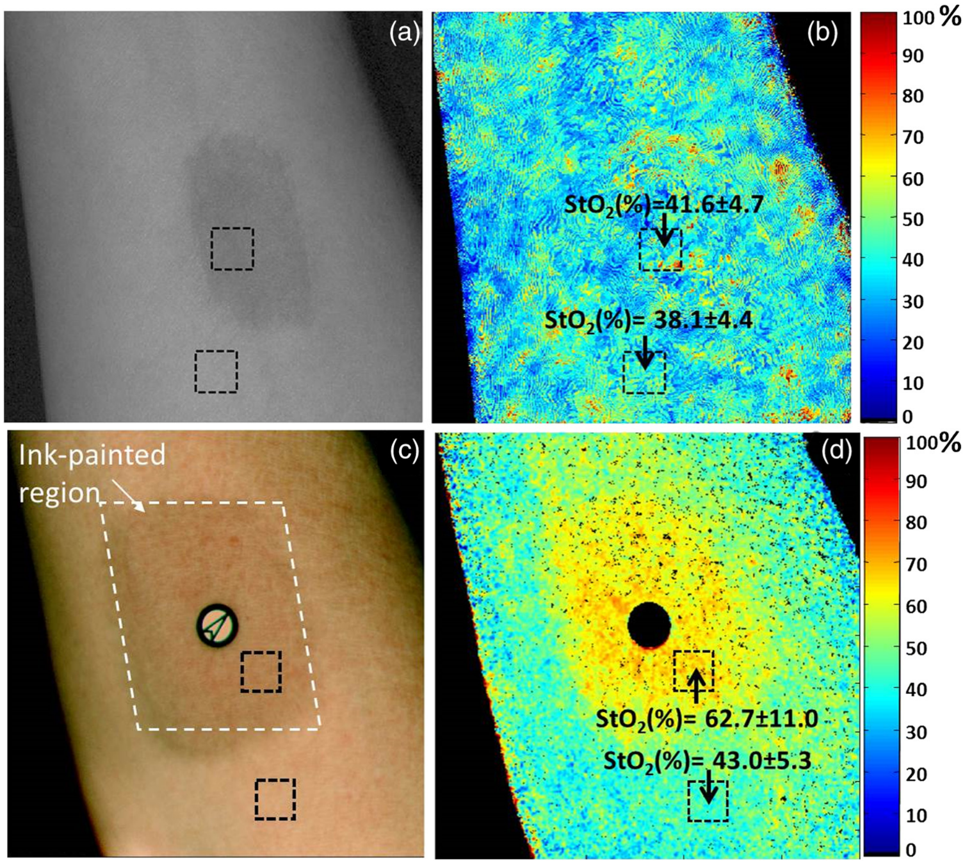

Fig. 8 Oxygenation of skin partially painted with ink. (a) and (c) Picture of the arm with a portion of skin painted with ink. (b) Oxygenation map generated by our multispectral imaging system. (d) Oxygenation map generated by a commercial hyperspectral imaging system.

an important indicator of skin tissue viability, the proposed StO_2 imaging technique may be used in many clinical applications, such as plastic surgery, organ transplantation, and wound healing. The limitation of this imaging technique is that it may eliminate the lower-order heterogeneities of skin tissue, leading to the diminished structural features. By projecting different patterns of illumination, defining different imaging algorithms, and choosing different wavelength sets, it is also possible to use the multispectral imaging system for noncontact imaging of skin tissue hemoglobin concentration, scattering, and melanin concentration. Characterization of these additional functional parameters may help to identify angiogenesis, bleeding, size change of cell nucleus, and other tissue anomalies. A Monte Carlo model was used to simulate light propagation in skin tissue. Our Monte Carlo simulation result showed that the averaged interrogation depth is 1 to 2 mm and is as deep as reticular dermis, depending on the blood concentration, melanin, and scattering level in the skin. The simulation results were then fit into a semi-infinite diffusion model in order to derive an analytical expression of SDR for effective reconstruction of tissue StO_2. The above approximations may introduce a systemic error in StO_2 reconstruction. First of all, the Monte Carlo model assumed homogenous tissue properties in each layer while typical skin tissue has a lateral heterogeneity. Second, the diffusion approximation assumes a turbid medium where the reduced scattering coefficient is much greater than the absorption coefficient. This is not always true in multilayer skin tissue. Finally, both the epidermis and the dermis layers of skin are very thin, leading to the breakup of diffuse approximation for light with a short penetration depth. In order to minimize the effect of these artifacts on the accuracy of StO_2 measurement, our multispectral oxygen imaging algorithm defined the correlation between the Monte Carlo model and the analytical solutions in advance based on the simulated data.

Two major measurement artifacts involved in our *in vivo* experiments of skin tissue StO_2 imaging are motion artifact and the artifact caused by the arm curvature. In our study, the motion artifact was minimized by keeping the subject's arm steady during the entire test period since a complete cycle of multispectral imaging at six wavelengths took around 2 s. An image processing algorithm was used to examine whether the arm location was maintained stable among the acquired six images. The measurement was considered invalid if there is a shift of the arm location. In terms of the artifact caused by the arm curvature, it mainly presents at the edge of the arm, as shown in Fig. 4. Currently, we do not have an effective calibration method to correct this artifact. To further reduce this artifact, we may consider profilometry correction using a tissue-simulating phantom[48] or by wrapping a paper mask on the curve arm for calibration.[49]

Although wide-gap second derivative spectroscopy has been proposed for tissue oxygenation measurement for a while,[45] we are the first to implement it for multispectral imaging of cutaneous tissue StO_2. Compared with probe technologies that provide single-point measurements of oxygenation, our multispectral imaging technique has the advantage of noncontact measurement as well as less intrapatient variability since it provides oxygenation mapping of an area of skin. Compared with other hyperspectral imaging systems, our technique has the advantage of higher temporal resolution since the StO_2 reconstruction algorithm requires multispectral images at only a small number of wavelengths. We have previously explored the SDR algorithm based on four wavelengths.[50] In comparison with our previous work, six wavelengths are selected in our current imaging algorithm so that more spectral characteristics of oxy- and deoxy-hemoglobin can be captured in SDR calculation. These six wavelengths are optimized for not only improved sensitivity to tissue oxygenation changes but also clinical utility and engineering feasibility. Currently, our multispectral imaging system is able to achieve an overall temporal resolution of 2 s per measurement and a typical postprocessing speed of 30 s per measurement, depending on the spatial resolution of the StO_2 map. These figures can be significantly improved by optimizing and customizing the engineering design of the imaging system.

In this study, skin StO_2 of 10 subjects with different skin types was measured to evaluate the effect of skin type on our multispectral measurement of oxygenation. Since the reflectance spectra of all StO_2 levels are almost overlapped with each other at the high melanin level, it is possible that the measurement bias is hard to reduce for patients with very dark skin. Extensive human tests with different skin colors are necessary in order to evaluate the robustness and clinical utility of the proposed imaging algorithm.

4 Conclusion

This paper reports a multispectral imaging algorithm for cutaneous tissue StO_2 mapping with minimal bias induced by skin conditions. A mathematical model is first established to simulate skin tissue reflectance spectra at different conditions, including skin oxygen saturation, blood concentration, tissue scattering, and melanin concentration. Based on the simulation results, the SDR parameter is derived and the optimal wavelength set of 544, 552, 568, 576, 592, and 600 nm is obtained for multispectral reconstruction of tissue StO_2 regardless of tissue variations. The proposed multispectral imaging algorithm is verified by benchtop and *in vivo* experiments. The benchtop experiment shows that the reconstructed StO_2 map is not vulnerable to variations in blood concentration, scattering, and background absorption levels. The *in vivo* experiment shows that the proposed multispectral imaging algorithm is able to monitor cutaneous tissue StO_2 at a sampling rate of 0.5 Hz. The test of 10 human subjects with different skin types shows that skin type does not have significant effect on our StO_2 measurement. We also show that the reconstructed StO_2 map by the multispectral imaging algorithm is less affected by skin background absorption compared with the OxyVu hyperspectral imaging system. Our experimental results indicate that the proposed multispectral imaging technique has the potential for quantitative imaging of skin tissue StO_2 dynamics with minimal artifacts at different skin conditions. Further *in vivo* validation tests are necessary before implementation of the proposed multispectral imaging algorithm in a clinical setting.

Appendix A: Absorption Weight Factors Determination by Matching Diffuse Transport Model and Monte Carlo Model

As described in Eq. (9) in Sec. 2.1.1, a weight factor f was used to calculate the averaged overall absorption of the whole skin. This weight factor indicates how the absorption of a specific layer contributes to the overall absorption of skin. The weight factor was found by matching the skin spectral reflectance simulated by the diffuse transport model with the reflectance simulated by the Monte Carlo model. The diffuse transport model has been described in Sec. 2.1.1, and the Monte Carlo model is described here.

A Monte Carlo simulation of photon migration in a seven-layer tissue model was used to simulate spectral reflectance of skin of different conditions. A Monte Carlo Simulation Package, developed in Ref. 39, was used with the following input parameters for each tissue layer: thickness d, refractive index n, anisotropy factor g, absorption $\mu_a(\lambda)$, and scattering $\mu_s(\lambda)$. The values of d, n, and g of each layer are listed in Table 1. The values of n and g here are measured in 633 nm and they are considered as constants for approximation in this simulation. The absorption coefficient $\mu_a(\lambda)$ of each layer was calculated using the same algorithm as in the diffuse model [Eqs. (1) to (8)]. The scattering $\mu_s(\lambda)$ of each layer, which was calculated differently compared to the diffuse model, is explicitly described here.

The scattering coefficient μ_s of each layer measured at 633 nm is listed in Table 1. But there is no published data of μ_s versus λ for each skin layer. Thus, the following method was used to approximate the wavelength-dependent μ_s for each skin layer. Tseng et al.[23] reported that the reduced scattering coefficient of *in vivo* skin can be expressed as

$$\mu_S'(\lambda < 600\,\text{nm}) = a_1\lambda^{-b_1}\,(\text{cm}^{-1}) \quad (b_1 = 1.35\text{ to }1.6), \tag{19}$$

$$\mu_s'(\lambda > 600\,\text{nm}) = a_2\lambda^{-b_2}\,(\text{cm}^{-1}) \quad (b_2 = 1.00\text{ to }1.15). \tag{20}$$

These two equations were solved using the μ_s (633 nm) values listed in Table 1 to get parameters a_1 and a_2 (fixed $b_1 = 1.5$ and $b_2 = 1.07$) for each skin layer.

The scattering of the hypodermis, which is very different from other layers, is given by[44]

$$\mu_s' = 1050.6 \cdot \lambda^{-0.68}. \tag{21}$$

Finally, the d, n, g, $\mu_a(\lambda)$, and $\mu_s'(\lambda)$ of each layer were fed into the Monte Carlo simulation package. 200 K photons were used for a single simulation. The skin spectral reflectance of different skin conditions are simulated using the above Monte Carlo method.

Then the weight factors for seven skin layers in the diffuse transport model will be determined by matching the skin reflectance simulated by the diffuse model with the reflectance simulated by the Monte Carlo method. This problem can be represented by the nonlinear least square optimization problem below. The optimal weight factors are found when the square error between the reflectance of two models is minimized.

Decision variable: weight factor f_i ($i = 1$ to 7)
Objective function: Minimize $\sum_\lambda \{R[\mu_a(f_i)] - R_{\text{MC}}\}^2$
Constraints: $\sum_i f_i = 1$ and $0 \le f_i \le 1$ ($i = 1$ to 7)

$R[\mu_a(f_i)]$ is the spectral reflectance calculated using the diffuse model, and R_{MC} is the spectral reflectance simulated using the Monte Carlo method.

This optimization problem was solved by a trust-region-reflective algorithm using MATLAB®. Different weight factors are derived for different skin conditions.

Appendix B: Analytical Expression of SDR ~ StO$_2$

Taking the second derivative of $r(= \mu_a/\mu_s')$ as a function of wavelength λ, one will get

$$\frac{\mathrm{d}^2 r}{\mathrm{d}\lambda^2} = A \cdot \frac{\mathrm{d}^2\mu_a}{\mathrm{d}\lambda^2} + B \cdot \frac{\mathrm{d}\mu_a}{\mathrm{d}\lambda} + C \cdot \mu_a, \tag{22}$$

where

$$A = (1/\mu_s'); \quad B = -(2/\mu_s'^2)\left(\frac{\mathrm{d}\mu_s'}{\mathrm{d}\lambda}\right);$$

$$C = \frac{1}{\mu_s'^2}\left[\frac{2}{\mu_s'}\left(\frac{d\mu_s'}{d\lambda}\right)^2 - \frac{\mathrm{d}^2\mu_s'}{\mathrm{d}\lambda^2}\right].$$

Since $\mu_s' = a\lambda^{-4} + b\lambda^{-0.22}$ ($a = 1.1 \times 10^{12}$; $b = 73.7$) for *in vivo* skin, one can find that the second and third terms in Eq. (22) are much smaller than the first term. Thus,

$$\frac{\mathrm{d}^2 r}{\mathrm{d}\lambda^2} \approx \frac{1}{\mu_s'} \cdot \frac{\mathrm{d}^2\mu_a}{\mathrm{d}\lambda^2}.$$

Since $\mu_a = \sum_{i=1}^{7} \mu_{ai} \cdot f_i$, where $\mu_{ai} = \mu_{ai}^{\text{HbO}} + \mu_{ai}^{\text{Hb}} + \mu_{ai}^{\text{mel}} + \mu_{ai}^{\text{water}} + \mu_{ai}^{\text{fat}} + \mu_{ai}^{\text{base}}$, substituting each absorption term using Eqs. (2) to (7), one will get

$$\begin{aligned}\mu_a &= F^{\text{Hbt}} \cdot \varepsilon^{\text{HbO}} \cdot \text{StO}_2 + F^{\text{Hbt}} \cdot \varepsilon^{Hb} \cdot (1 - \text{StO}_2)\\ &\quad + F^{\text{mel}} \cdot \varepsilon^{\text{mel}} + F^{\text{water}} \cdot \varepsilon^{\text{water}} + F^{\text{fat}} \cdot \varepsilon^{\text{fat}} + F^{\text{base}} \cdot \varepsilon^{\text{base}},\end{aligned}$$

where

$$F^{\text{Hbt}} = \left(2.303\,\frac{C_{\text{Hb}}}{\text{M.W.}_{\text{Hb}}}\sum_{i=1}^{7} C_i^{\text{blood}} \cdot f_i\right),$$

$$F^{\text{mel}} = \sum_{i=1}^{7} C_i^{\text{mel}} \cdot f_i$$

$$F^{\text{water}} = \sum_{i=1}^{7} C_i^{\text{water}} \cdot (1 - r_i C_i^{\text{blood}}) \cdot f_i,$$

$$F^{\text{fat}} = \sum_{i=1}^{7} C_i^{\text{fat}} \cdot (1 - r_i C_i^{\text{blood}}) \cdot f_i$$

$$F^{\text{base}} = \sum_{i=1}^{7} (1 - C_i^{\text{blood}} - C_i^{\text{mel}} - C_i^{\text{fat}})(1 - r_i C_i^{\text{blood}}) \cdot f_i.$$

The absorption of fat and water are small terms. Thus,

$$\begin{aligned}\mu_a &\approx F^{\text{Hbt}} \cdot \varepsilon^{\text{HbO}} \cdot \text{StO}_2 + F^{\text{Hbt}} \cdot \varepsilon^{\text{Hb}} \cdot (1 - \text{StO}_2)\\ &\quad + F^{\text{mel}} \cdot \varepsilon^{\text{mel}} + F^{\text{base}} \cdot \varepsilon^{\text{base}}.\end{aligned}$$

Thus,

$$\begin{aligned}\frac{\mathrm{d}^2 r}{\mathrm{d}\lambda^2} &\approx \frac{1}{\mu_s'}\left[F^{\text{Hbt}}\frac{\mathrm{d}^2\varepsilon^{\text{HbO}}}{\mathrm{d}\lambda^2} \cdot \text{StO}_2 + F^{\text{Hbt}}\frac{\mathrm{d}^2\varepsilon^{\text{Hb}}}{\mathrm{d}\lambda^2} \cdot (1 - \text{StO}_2)\right.\\ &\quad \left. + F^{\text{mel}}\frac{\mathrm{d}^2\varepsilon^{\text{mel}}}{\mathrm{d}\lambda^2} + F^{\text{base}}\frac{d^2\varepsilon^{\text{base}}}{d\lambda^2}\right].\end{aligned}$$

It is found that $(\mathrm{d}^2\varepsilon^{\text{mel}})/(\mathrm{d}\lambda^2)$, $(\mathrm{d}^2\varepsilon^{\text{base}})/(\mathrm{d}\lambda^2) \ll (\mathrm{d}^2\varepsilon^{\text{HbO}})/(\mathrm{d}\lambda^2)$, $(\mathrm{d}^2\varepsilon^{\text{Hb}})/(\mathrm{d}\lambda^2)$ [since $\varepsilon^{\text{mel}}(\lambda)$ and $\varepsilon^{\text{base}}(\lambda)$ have an exponential decay shape]. Thus,

$$\frac{\mathrm{d}^2 r}{\mathrm{d}\lambda^2} \approx \frac{F^{\mathrm{Hbt}}}{\mu_s'} \left[\frac{\mathrm{d}^2 \varepsilon^{\mathrm{HbO}}}{\mathrm{d}\lambda^2} \cdot \mathrm{StO}_2 + \frac{\mathrm{d}^2 \varepsilon^{\mathrm{Hb}}}{\mathrm{d}\lambda^2} \cdot (1 - \mathrm{StO}_2) \right]. \tag{23}$$

Thus, the second derivative ratio (SDR) is

$$\begin{aligned} \mathrm{SDR} &= \frac{rr(\lambda_1)''}{rr(\lambda_2)''} \\ &= \frac{\mu_s'(\lambda_2)}{\mu_s'(\lambda_1)} \cdot \frac{[(\varepsilon^{\mathrm{HbO}})''_{\lambda_1} - (\varepsilon^{\mathrm{Hb}})''_{\lambda_1}]\mathrm{StO}_2 + (\varepsilon^{\mathrm{Hb}})''_{\lambda_1}}{[(\varepsilon^{\mathrm{HbO}})''_{\lambda_2} - (\varepsilon^{\mathrm{Hb}})''_{\lambda_2}]\mathrm{StO}_2 + (\varepsilon^{\mathrm{Hb}})''_{\lambda_2}}. \end{aligned} \tag{24}$$

This is the approximated analytical expression of SDR for any λ_1 and λ_2.

Acknowledgments

This project was sponsored by National Institute of Standards and Technology (60NANB10D184), National Institute of Health (HL073087, GM 077185, and GM 069589), US Army Medical Research Acquisition Act (W81XWH-11-2-0142), and Natural Science Foundation of China (81271527).

References

1. H. D. Sostman et al., "Evaluation of BA1112 rhabdomyosarcoma oxygenation with microelectrodes, optical spectrophotometry, radiosensitivity, and magnetic resonance spectroscopy," *Magn. Reson. Med.* **20**(2), 253–267 (1991).
2. M. R. Pinsky, "Functional haemodynamic monitoring," *Curr. Opin. Crit. Care* **20**(3), 288–293 (2014).
3. M. Sentjurc, M. Cemazar, and G. Sersa, "EPR oximetry of tumors in vivo in cancer therapy," *Spectrochim. Acta A Mol. Biomol. Spectrosc.* **60**(6), 1379–1385 (2004).
4. B. Chance, "Current state of methodology on hemoglobin oximetry in tissues," *Adv. Exp. Med. Biol.* **345**, 23–32 (1994).
5. R. F. Lohman et al., "Predicting skin flap viability using a new intraoperative tissue oximetry sensor: a feasibility study in pigs," *J. Reconstr. Microsurg.* **30**(6), 405–412 (2014).
6. E. M. Nemoto, H. Yonas, and A. Kassam, "Clinical experience with cerebral oximetry in stroke and cardiac arrest," *Crit. Care Med.* **28**(4), 1052–1054 (2000).
7. M. M. Said, N. Niforatos, and K. Rais-Bahrami, "Validation of near infrared spectroscopy to measure abdominal somatic tissue oxygen saturation in neonates," *J. Neonatal Perinatal Med.* **6**(1), 23–30 (2013).
8. D. A. Benaron et al., "Design of a visible-light spectroscopy clinical tissue oximeter," *J. Biomed. Opt.* **10**(4), 044005 (2005).
9. T. Durduran et al., "Bulk optical properties of healthy female breast tissue," *Phys. Med. Biol.* **47**(16), 2847–2861 (2002).
10. R. X. Xu et al., "A prospective pilot clinical trial evaluating the utility of a dynamic near-infrared imaging device for characterizing suspicious breast lesions," *Breast Cancer Res.* **9**(6), R88 (2007).
11. N. Shah et al., "Spatial variations in optical and physiological properties of healthy breast tissue," *J. Biomed. Opt.* **9**(3), 534–540 (2004).
12. B. J. Tromberg et al., "Non-invasive in vivo characterization of breast tumors using photon migration spectroscopy," *Neoplasia* **2**(1–2), 26–40 (2000).
13. S. A. Shah et al., "Cutaneous wound analysis using hyperspectral imaging," *Biotechniques* **34**(2), 408–413 (2003).
14. J. T. Nguyen et al., "A novel pilot study using spatial frequency domain imaging to assess oxygenation of perforator flaps during reconstructive breast surgery," *Ann. Plast. Surg.* **71**(3), 308–315 (2013).
15. D. Jakovels and J. Spigulis, "2-D mapping of skin chromophores in the spectral range 500–700 nm," *J. Biophotonics* **3**(3), 125–129 (2010).
16. J. M. Kainerstorfer et al., "Principal component model of multispectral data for near real-time skin chromophore mapping," *J. Biomed. Opt.* **15**(4), 046007 (2010).
17. I. Nishidate et al., "Visualizing of skin chromophore concentrations by use of RGB images," *Opt. Lett.* **33**(19), 2263–2265 (2008).
18. K. J. Zuzak et al., "Visible reflectance hyperspectral imaging: characterization of a noninvasive, in vivo system for determining tissue perfusion," *Anal. Chem.* **74**(9), 2021–2028 (2002).
19. K. J. Zuzak et al., "Active DLP hyperspectral illumination: a noninvasive, in vivo system characterization visualizing tissue oxygenation at near video rates," *Anal. Chem.* **83**(19), 7424–7430 (2011).
20. A. Bjorgan, M. Milanic, and L. L. Randeberg, "Estimation of skin optical parameters for real-time hyperspectral imaging applications," *J. Biomed. Opt.* **19**(6), 066003 (2014).
21. T. Lister, P. A. Wright, and P. H. Chappell, "Optical properties of human skin," *J. Biomed. Opt.* **17**(9), 090901 (2012).
22. M. Hajizadeh-Saffar, J. W. Feather, and J. B. Dawson, "An investigation of factors affecting the accuracy of in vivo measurements of skin pigments by reflectance spectrophotometry," *Phys. Med. Biol.* **35**, 1301 (1990).
23. S. H. Tseng et al., "Chromophore concentrations, absorption and scattering properties of human skin in-vivo," *Opt. Express* **17**(17), 14599–14617 (2009).
24. S. H. Tseng, A. Grant, and A. J. Durkin, "In vivo determination of skin near-infrared optical properties using diffuse optical spectroscopy," *J. Biomed. Opt.* **13**, 014016 (2008).
25. I. S. Seo, P. R. Bargo, and N. Kollias, "Simultaneous assessment of pulsating and total blood in inflammatory skin lesions using functional diffuse reflectance spectroscopy in the visible range," *J. Biomed. Opt.* **15**, 060507 (2010).
26. G. N. Stamatas, M. Southall, and N. Kollias, "In vivo monitoring of cutaneous edema using spectral imaging in the visible and near infrared," *J. Investig. Dermatol.* **126**(8), 1753–1760 (2006).
27. G. N. Stamatas et al., "Noninvasive measurements of skin pigmentation in situ," *Pigment Cell Res.* **17**(6), 618–626 (2004).
28. J. R. Mansfield et al., "Analysis of spectroscopic imaging data by fuzzy C-means clustering," *Anal. Chem.* **69**(16), 3370–3374 (1997).
29. R. Gillies et al., "Systemic effects of shock and resuscitation monitored by visible hyperspectral imaging," *Diabetes Technol. Ther.* **5**(5), 847–855 (2003).
30. L. C. Cancio et al., "Hyperspectral imaging: a new approach to the diagnosis of hemorrhagic shock," *J. Trauma* **60**(5), 1087 (2006).
31. M. G. Sowa et al., "Spectroscopic assessment of cutaneous hemodynamics in the presence of high epidermal melanin concentration," *Clin. Chim. Acta* **317**(1–2), 203–212 (2002).
32. J. C. Harsanyi and C. I. Chang, "Hyperspectral image classification and dimensionality reduction: an orthogonal subspace projection approach," *IEEE Trans. Geosci. Remote Sens.* **32**(4), 779–785 (1994).
33. I. Nishidate et al., "Noninvasive spectral imaging of skin chromophores based on multiple regression analysis aided by Monte Carlo simulation," *Opt. Lett.* **36**(16), 3239–3241 (2011).
34. I. Nishidate et al., "Noninvasive imaging of human skin hemodynamics using a digital red-green-blue camera," *J. Biomed. Opt.* **16**(8), 086012 (2011).
35. P. Di Ninni, F. Martelli, and G. Zaccanti, "The use of India ink in tissue-simulating phantoms," *Opt. Express* **18**(26), 26854–26865 (2010).
36. I. V. Meglinski and S. J. Matcher, "Quantitative assessment of skin layers absorption and skin reflectance spectra simulation in the visible and near-infrared spectral regions," *Physiol. Meas.* **23**, 741 (2002).
37. I. V. Meglinski and S. J. Matcher, "Computer simulation of the skin reflectance spectra," *Comput. Methods Programs Biom.* **70**(2), 179–186 (2003).
38. S. L. Jacques, R. D. Glickman, and J. A. Schwartz, "Internal absorption coefficient and threshold for pulsed laser disruption of melanosomes isolated from retinal pigment epithelium," *Proc. SPIE* **2681**, 468 (1996).
39. L. Wang, S. L. Jacques, and L. Zheng, "MCML–Monte Carlo modeling of light transport in multi-layered tissues," *Comput. Methods Programs Biomed.* **47**(2), 131–146 (1995).
40. S. A. Prahl, "Simple and accurate approximations for reflectance from a semi-infinite turbid medium," in *Biomedical Topical Meeting*, pp. 613–615, Optical Society of America, Florida (2002).
41. Oregon Medical Laser Center, "Optical Properties Spectra," (2015), http://omlc.ogi.edu/spectra (2 2015).
42. H. Buiteveld, J. H. M. Hakvoort, and M. Donze, "Optical properties of pure water," *Proc. SPIE* **2258**, 174 (1994).

43. I. S. Saidi, "Transcutaneous optical measurement of hyperbilirubinemia in neonates," PhD Thesis, Rice University (1992).
44. A. N. Bashkatov et al., "Optical properties of human skin, subcutaneous and mucous tissues in the wavelength range from 400 to 2000 nm," *J. Phys. D: Appl. Phys.* **38**, 2543 (2005).
45. D. E. Myers et al., "Noninvasive method for measuring local hemoglobin oxygen saturation in tissue using wide gap second derivative near-infrared spectroscopy," *J. Biomed. Opt.* **10**, 034017 (2005).
46. T. Jarm et al., "Postocclusive reactive hyperemia in healthy volunteers and patients with peripheral vascular disease measured by three noninvasive methods," *Adv. Exp. Med. Biol.* **530**, 661 (2003).
47. R. L. Greenman et al., "Early changes in the skin microcirculation and muscle metabolism of the diabetic foot," *Lancet* **366**(9498), 1711–1717 (2005).
48. S. Gioux et al., "Three-dimensional surface profile intensity correction for spatially modulated imaging," *J. Biomed. Opt.* **14**(3), 034045 (2009).
49. J. M. Kainerstorfer et al., "Quantitative principal component model for skin chromophore mapping using multi-spectral images and spatial priors," *Biomed. Opt. Express* **2**(5), 1040–1058 (2011).
50. R. X. Xu et al., "Dual-mode imaging of cutaneous tissue oxygenation and vascular thermal reactivity," *J. Vis. Exp.* (46), e2095 (2010).

Jiwei Huang earned his BS degree from Sun Yat-Sen University and a PhD degree from the Lab of Multimodal Imaging and Image-Guided Therapy of The Ohio State University. Currently, he works in the semiconductor industry in R&D of optical microcopy systems. He is a scientist and engineer with expertise in optical microscopic imaging, fluorescence spectroscopy and imaging, low-photon-flux detection system, hyperspectral imaging system and algorithm, tissue optics model, oximetry, and imaging contrast agents.

Shiwu Zhang is currently an associate professor in the Department of Precision Machinery and Precision Instrumentation, USTC. He has also been a postdoctoral research fellow in the Department of Computer Science, Hong Kong Baptist University, Hong Kong. He has worked in a number of research programs sponsored by the National Science Foundation of China, Chinese Academy of Sciences, Chinese State High-Tech Development Plan, etc. His current research interests include biomedical optics and intelligent robot.

Surya Gnyawali has a PhD degree in biophysics and works in biomedical imaging. He is a research scientist at the Department of Surgery, The Ohio State University Medical Center. He has published over 20 scientific publications.

Chandan K. Sen is a tenured professor of surgery, executive director of The Ohio State University Comprehensive Wound Center, and director of the Ohio State University's Center for Regenerative Medicine and Cell-Based Therapies. He is also the associate dean for research at The Ohio State University Wexner Medical Center. He and his team have published over 300 scientific publications. He has a H-index of 74 and is currently cited approximately 2000 times every year.

Ronald X. Xu is an associate professor of biomedical engineering at The Ohio State University and a professor of precision machinery and instrumentation at the University of Science and Technology of China. He has published over 80 technical papers in biomedical imaging, drug delivery, and three-dimensional printing. In 2010, he was honored as one of the 10 brightest Central Ohioans by Columbus CEO Magazine. In 2011, he was awarded the TechColumbus "Inventor of the Year" Award.